

## Supplementary Information

### Supplementary Materials and Methods:

#### Fabrication of substrate with microscale gratings

The surface structures on the bottom substrate were prepared by micromachining a silicon wafer. After patterning parallel stripes of photoresist (AZ5214) with a pitch (i.e., periodicity) of 200  $\mu\text{m}$  and solid fractions  $\phi_s$  varying from 0.2 to 0.8 on a 400-500  $\mu\text{m}$ -thick, 4-inch, and (100)-type silicon wafer by photolithography, deep reactive ion etching (DRIE) was used to form 50  $\mu\text{m}$ -deep trenches into the silicon. After removing the photoresist, a layer of 2  $\mu\text{m}$ -thick Teflon<sup>®</sup> AF 1600 was spin-coated on the wafer to turn the entire surface hydrophobic.

#### Fabrication of top plate with hydrophilic rectangular pattern

The wetting pattern on the top plate was prepared on a glass slide. After spin-coating a photoresist (AZ4620), which is hydrophobic, on a 1 mm-thick plain microscope slide of 7.6 cm by 2.5cm (Fisher Scientific 12-549-3), a rectangular window of 2.5 mm by 15 mm was opened by photolithography to expose the underlying hydrophilic glass surface.

#### Dynamic contact angle measurements

As illustrated in Fig. 2, the superhydrophobic silicon substrate was mounted on a moving stage, while the glass top plate was stationary and held the droplet at a fixed position always visible to the camera. As the substrate slid to the left, the water droplet traversed the line patterns on the substrate to the right (relatively). During the droplet sliding, both advancing and receding contact angles could be captured. By aligning the viewing direction parallel to the line pattern and perpendicular to the moving direction, the captured images of contact line motion was maintained close to a 2-D condition. In order to observe details of contact line motion, which includes jumping from one surface structure to the next in a near 2-D condition, a high-speed camera (Vision Research Phantom V7.2) was employed at a rate up to 6000 frames per second (fps).

## Supplementary Discussions with Figures S1-S5 and Table S1:

### Local contact angles during 2-D contact-line receding

Figure S1 shows the local (i.e., microscopic) contact angle of a receding 2-D contact line measured over time in two different time scales, adapted from Chen<sup>24</sup>. The left graph shows around 4 cycles (captured at 300 fps), illustrating the discontinuous nature of the contact line receding on a structured surface. Similar plots have been reported based on simulation results<sup>36,37</sup>, which described periodic “stick-slip-jump” contact line motions. Using a much smaller time scale captured at 6000 fps, the right graph shows one cycle to provide more details when the receding contact line jumps. The sudden increase in the contact angle represents the receding contact line being detached from one structure and pinned on the next structure.

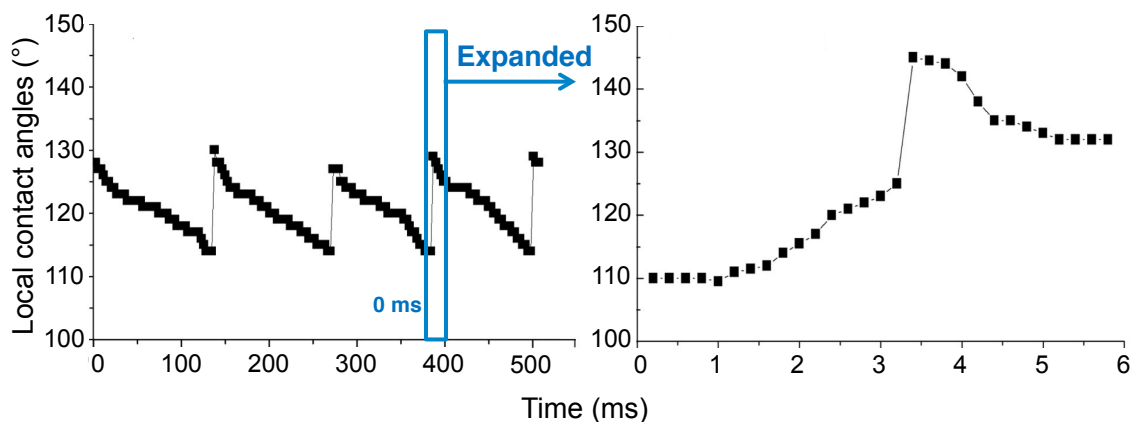


**Figure S1.** Local/microscopic receding contact angle as a function of time measured from high-speed images of 2-D contact-line receding.

### Influence of the top plate distance on the recovery of the apparent contact angle

Figure S2 illustrates how the apparent angle recovery, i.e., the stage 4 observed in the experiment, would vanish if the top plate were placed far away to represent a true (albeit imaginary) 2-D scenario. The figure considers a top plate placed at three different distances  $z_1$ ,  $z_2$ , and  $z_\infty$  from the substrate and ignores the microscopic details to focus on

the apparent contact angles the menisci form between the top plates and bottom substrate (blue lines). Starting from the initial meniscus with  $\theta_R^*$  (blue solid line) common to all three plate distances of  $z_1$ ,  $z_2$ , and  $z_\infty$ , the contact lines would slide and jump to the next structure, resulting in three new menisci (blue dotted lines) marked as ①, ②, and  $\infty$ , respectively. Because the menisci would be pinned at different heights  $z_1 < z_2 < z_\infty$ , we would have  $\theta_1^* > \theta_2^* > \theta_\infty^* = \theta_R^*$ . In other words, if the top plate were placed farther away from the microstructured surface, the apparent angle of the meniscus pinned on the top plate would deviate less from the apparent receding angle on structured surface at the bottom. If the top plate were infinitely far away (i.e., the true 2-D case), the deviation would wane and recovery stage (i.e., stage 4 observed in experiment) would vanish.

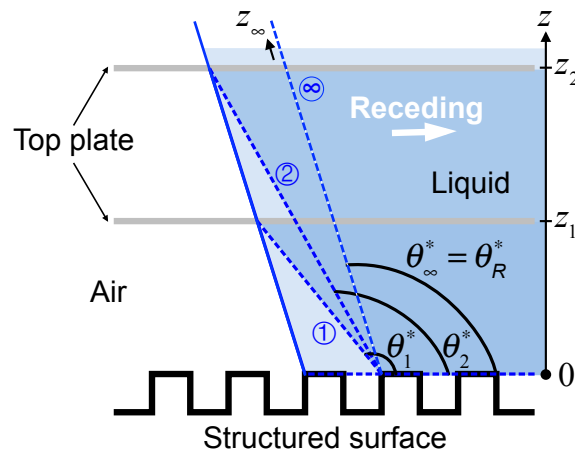


**Figure S2.** Illustration to show the meniscus pinned on the top plate causes the apparent contact angle to be different from the apparent receding angle. Because in practice the top plate is placed at a finite distance from the structured surface at the bottom, i.e.,  $z = z_1$  or  $z_2$ , the apparent angle increases when the meniscus jumps to the next structure, i.e., from the blue solid line to the blue dashed lines. This increase of the apparent angle by the meniscus jumping would diminish as the top plate is placed farther away, so that for  $z = z_\infty$  the apparent angle would stay the same as the apparent receding angle.

### Definition and calculation of line solid fraction

In analogy to the areal solid fraction  $\phi_s$  defined by Cassie and Baxter<sup>1</sup>, i.e., the ratio of real solid-liquid (two-phase) contact area to the apparent (projected) area, we define the line solid fraction  $\lambda_s$  to be the ratio of real solid-liquid-air (three-phase) contact line  $\hat{l}_s$  to the apparent (projected) line  $l$ , as follows:

$$\lambda_s = \frac{\hat{l}_s}{l} \quad (\text{S1})$$

Because the period of the contact line pinned on the solid (measured to be ~97% of time in the 2-D experiment) dominates the period of sliding on solid and air (measured to be ~3% of time in the 2-D experiment), the real contact line  $\hat{l}_s$  is determined by the contact line pinned on microstructures. Figure S3 depicts the contact line of a droplet receding on a square array of circular posts. The apparent/projected/macrosopic contact line of a sessile drop is circular on the structured surface (dashed red line on the right inset), while the real/local/microscopic contact line is intermittent and contorted (solid blue line in the left inset).

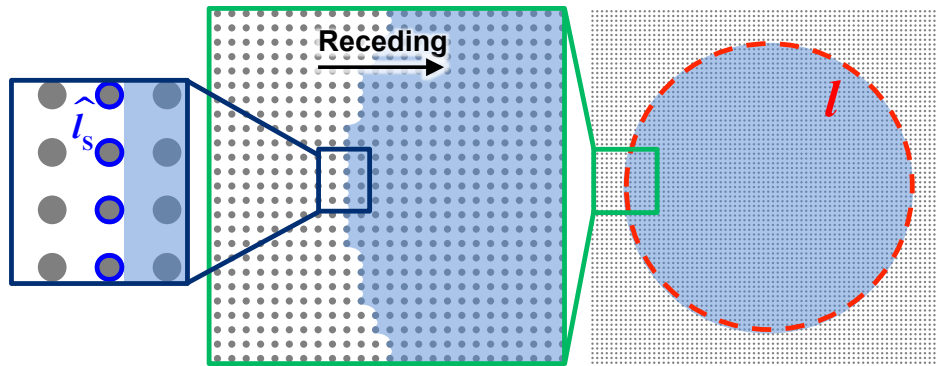


**Figure S3.** Line solid fraction defined as the ratio of the real contact line on solid ( $\hat{l}_s$ : blue solid lines in the inset) to the apparent contact line of the liquid on the structured surface ( $l$ : red dashed line). The figure shows the case of a sessile drop sliding on a square array of circular posts.

Normally it would be very difficult to calculate the real contact line and the apparent contact line exactly, because the relative size of the droplet and the microstructures also

affect their values. Furthermore, in the real world that is 3-D in nature, the local motion at each point of the contact line is affected by the neighboring points, and therefore the line solid fraction should be averaged over the contact line length of interest. Let us consider a segment of apparent contact line that forms angle  $\beta$  to the horizon (Fig. S4), and suppose the contact line is moving in direction  $\vec{v}$ , which forms angle  $\psi$  to the segment. Assuming the droplet is much larger than the microstructures (so that  $\beta$  is considered constant over multiple segments), the line solid fraction can be calculated as a spatial (i.e., angular) average of the line solid fraction of all segments over the contact line length of our interest, e.g., a circle for an entire spherical drop:

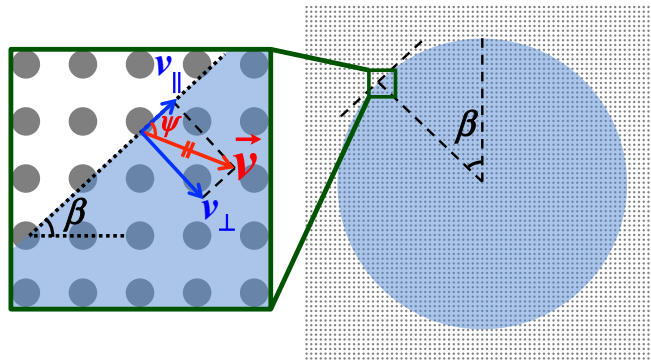
$$\lambda_s = \frac{1}{\beta_t} \int_0^{\beta_t} \lambda_s(\beta) \sin \psi d\beta \quad (\text{S2})$$

In the above equation,  $\lambda_s(\beta)$  is the ratio of the real contact line to the structural pitch at angle  $\beta$ , and  $\sin \psi$  accounts for the contact line resistance normal to the apparent contact line. The range of angle to be considered  $\beta_t$  is determined by the motion the contact line undergoes with. For the above case of Fig. S3, all the segments of the apparent contact line move towards the center of the droplet so that  $\psi = \pi/2$  and  $\beta_t = 2\pi$ , and we have:

$$\lambda_s = \frac{1}{2\pi} \int_0^{2\pi} \lambda_s(\beta) d\beta \quad (\text{S3})$$

However, for the cases of receding by droplet sliding, the segments of the tailing half of the apparent contact line recede with varying  $\psi$  so that  $\beta_t = \pi$  and  $\psi = \beta$ , and we have:

$$\lambda_s = \frac{1}{\pi} \int_0^{\pi} \lambda_s(\beta) \sin \beta d\beta \quad (\text{S4})$$



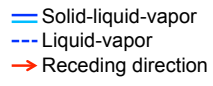
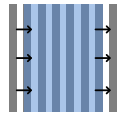
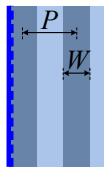
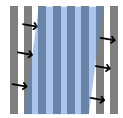
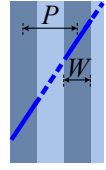
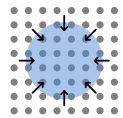
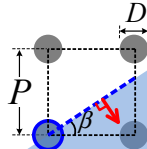
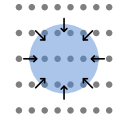
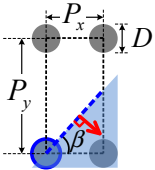
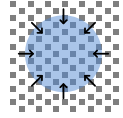
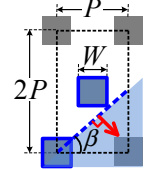
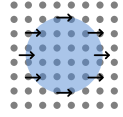
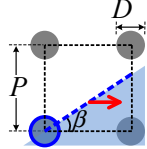
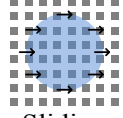
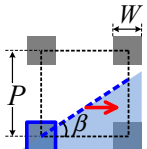
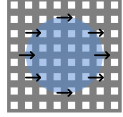
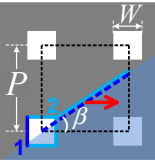
**Figure S4.** Contact line segment at angle  $\beta$  moving with angle  $\psi$  to the contact line

Table S1 presents  $\lambda_s$  derived for the various microstructures and receding conditions found in the literature. The averaged expression was simplified if there was symmetry in the considered range. Consider the case shown in Figs. S3 and S4 (i.e., Xu et al.<sup>31</sup> in Table S1) as an example, where all the segments of the apparent contact line of the droplet are receded by subtraction on a square array of circular posts. For one segment, the real contact line on solid is  $\pi D$ , and the effective pitch is  $P/\cos\beta$  for  $0 < \beta < \pi/4$  and  $P/\sin\beta$  for  $\pi/4 < \beta < \pi/2$ . Therefore, the line solid fraction can be calculated as:

$$\lambda_s = \frac{2}{\pi} \left( \int_0^{\pi/4} \frac{\pi D}{P/\cos\beta} d\beta + \int_{\pi/4}^{\pi/2} \frac{\pi D}{P/\sin\beta} d\beta \right) = \frac{2}{\pi} \frac{\pi D}{P} \sqrt{2} \quad (\text{S5})$$

Other cases can be derived in similar fashions, and their results are summarized in Table S1. For post structures, the real contact line is essentially the perimeter of the structure in the segment in consideration while the apparent contact line is the length of the “straight” apparent contact line at angle  $\beta$ . For hole structures, however, the real contact line is composed of two different cases: some recedes on solid where the receding contact angle is  $\theta_R$ , while some recedes across a hole where the receding contact angle is  $(\theta_R - 90^\circ)$ . When the circular posts are in a rectangular array<sup>19</sup>, one of the pitches and its apparent contact line termed as kinks<sup>19</sup> dominate the receding. When square posts are in a diamond-shape array (although the authors called it hexagonal array)<sup>13</sup>, the smallest repeating unit, i.e., a two-pitch by one-pitch rectangle, is considered.

**Table S1.** Line solid fraction  $\lambda_s$  used in Fig. 7 for different structures and receding conditions

	Receding conditions	Contact line segment	Line solid fraction $\lambda_s$	
This work	 Sliding		$\lambda_s = 1$	
Cassie <sup>1</sup>	 Sliding		$\lambda_s = \frac{W}{P}$	
Xu <sup>31</sup>	 Subtraction		$\lambda_s = \frac{2}{\pi} \frac{\pi D}{P} \sqrt{2}$	
Gauthier <sup>19</sup>	 Subtraction		$\lambda_s = \frac{2}{\pi} \frac{\pi D}{\sqrt{P_x^2 + P_y^2}} \left[ \tan^{-1} \left( \frac{P_y}{P_x} \right) + \left( \frac{P_x}{P_y} \right) \right]$	
Öner <sup>13</sup>	 Subtraction		$\lambda_s = \frac{2}{\pi} \frac{4W}{P} \sqrt{5}$	
Dufour <sup>7</sup>	 Sliding		$\lambda_s = \frac{2}{\pi} \frac{\pi D}{P} \left( \frac{1}{2} + \frac{\pi}{8} \right)$	
Priest <sup>12</sup>	 Sliding		$\lambda_s = \frac{2}{\pi} \frac{4W}{P} \left( \frac{1}{2} + \frac{\pi}{8} \right)$	
	 Sliding		$\lambda_{s_1} = \frac{W}{\pi P}, \theta_{R_1} = \theta_R - 90^\circ, \theta_{Y_1} = \theta_Y$ $\lambda_{s_2} = \frac{2}{\pi} \left( \frac{P-W}{P} + \frac{3W}{2P} + \frac{3W}{4P} \frac{\pi}{2} \right), \theta_{R_2} = \theta_R, \theta_{Y_2} = \theta_Y$	

Comparison of experimental 3-D data in the literature to existing models

Following Fig. 5, Fig. S5 compares each set of the 3-D data reported in the literature (red symbols) with the existing models in the literature (dashed lines) and our model (red solid line). The CB model for the static case is also included as a reference. While many existing models fit a certain set of experimental data, none of them fits all the data. In contrast, our model (i.e., Eq. 10 for gratings and posts and Eq. 11 for holes) fits all the data, giving a consistently good prediction of apparent receding contact angles regardless of the type and pattern of the surface structures and the condition of droplet moving.

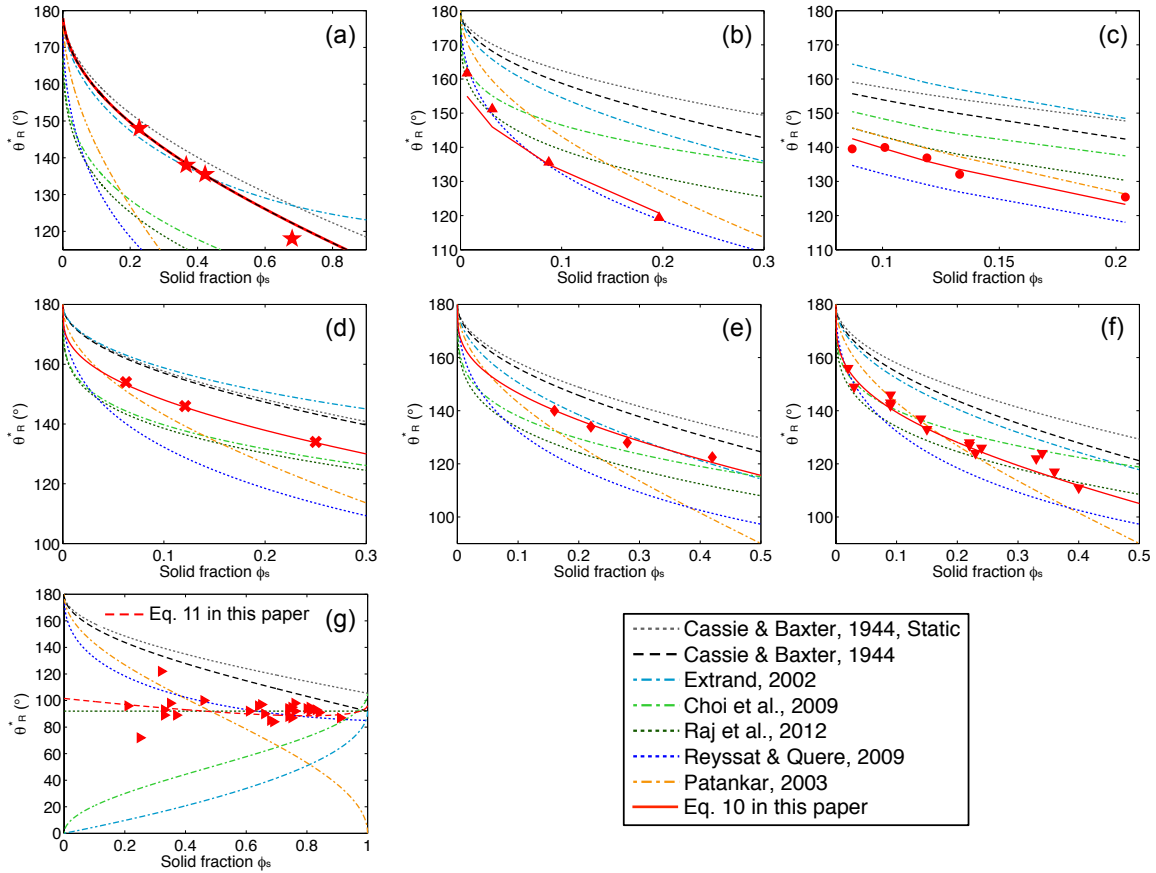


**Figure S5.** Experimental data (red symbols) of apparent receding contact angles in the literature, (a) Cassie<sup>1</sup> (b) Xu<sup>31</sup>, (c) Gauthier<sup>19</sup>, (d) Öner<sup>13</sup>, (e) Dufour<sup>7</sup>, (f) Priest<sup>12</sup>, and (g) holes in Priest<sup>12</sup>, each compared with the original and modified CB models in the literature (dashed lines) and the modified CB model of this paper (red solid line). For each figure, the model predictions were calculated from the experimental conditions used to obtain the data according to the reference. Only the model in this paper predicts all the experimental data consistently well.

Figure S5 warrants more details of how they were produced. For Fig. S5(a) (i.e., Cassie<sup>1</sup>), their model coincided with our Eq. 10, so they formed two overlapping lines. For Fig. S5(b) (i.e., Xu<sup>31</sup>), Eq. 8 was drawn using their experimentally measured static contact angle instead of theoretical values calculated from the CB model. For Fig S5(c) (i.e., Gauthier<sup>19</sup>), the graphs include only the prediction of rectangular arrays reported in their paper, because the solid fraction is controlled by two different pitches. For Fig. S5(d) (i.e., Öner<sup>13</sup>), the line fraction for the Extrand model<sup>3</sup> has only been given explicitly for such hexagonally-packed array. Lacking a general formula for other cases, a simple differential line fraction<sup>4</sup> was adopted for Extrand model in all other subfigures in Fig. S5. For Fig. S5(g), Eq. 11 (more generalized than Eq. 10) was used to predict apparent receding contact angles on hole structures.

**Table S2.** Summary of the models included in Fig. 5 and Fig. S5 for comparison

Approach		Theoretical expression	Notes
This work	Static apparent contact angle plus the time-average frictions acting on the TCL	$\cos\theta_R^* = \cos\theta^* + \sum_i (\cos\theta_{R_i} - \cos\theta_{Y_i}) \lambda_s$	$\cos\theta^*$ is the static apparent contact angle given by the general Cassie equation $\sum_i \phi_i \cos\theta_{Y_i}$ .
Cassie <sup>1</sup>	Linear average of contact angles on contact areas	$\cos\theta_R^* = \phi_s \cos\theta_R - \phi_g$	$\theta_R$ is the receding angle on solid; $\phi_s$ and $\phi_g$ are the solid and gas fraction determined by the advancing case.
Extrand <sup>3</sup>	Linear average of contact angles along TCL	$\theta_R^* = \lambda_p \theta_R + (1 - \lambda_p) \theta_{\text{air}}$	$\theta_{\text{air}} = 180^\circ$ ; $\lambda_p$ is the linear fraction of the contact line on asperities; the ideal Cassie state ( $\phi_s + \phi_g = 1$ ) is assumed.
Choi <sup>4</sup> Larsen <sup>16</sup>	Linear average of cosines of contact angles along TCL	$\cos\theta_R^* = r_\phi \phi_d \cos\theta_Y + (1 - \phi_d) \cos\theta_2$	$\theta_Y$ is the Young's angle on solid; $\phi_d$ is the differential area fraction at the receding meniscus; $r_\phi$ is the roughness coefficient for the liquid-solid interface; $\theta_2 = 180^\circ$ (stripes, posts) or $0^\circ$ (holes).
Raj <sup>5</sup>	Linear average of cosines of receding contact angles along TCL	$\cos\theta_R^* = \phi_{\text{max}} \cos\theta_R - (1 - \phi_{\text{max}})$	$\phi_{\text{max}} = D/P$ for receding on posts ( $D$ is diameter and $P$ is pitch); $\phi_{\text{max}} = 1$ for receding on holes.
Reyssat <sup>6</sup>	Lateral deformation of the receding meniscus	$\cos\theta_R^* - \cos\theta_A^* = \frac{a}{4} \phi_s \ln\left(\frac{\pi}{\phi_s}\right)$	$a = 3.8$ best fitted to data in Ref. 6; In theory, $a = 2$ ; $\phi_s$ is the solid fraction; $\theta_A^* = 180^\circ$ .
Patankar <sup>25</sup>	Liquid layer left on the receded structures	$\cos\theta_R^* = 2\phi_s - 1$	Original Cassie-Baxter equation with $\theta_R = 0^\circ$ and assuming the ideal Cassie state ( $\phi_s + \phi_g = 1$ ).

**Supplemental Movie S1-S3:**

MOVIE S1. Receding meniscus motion on structured surface ( $\phi_s = 0.5$ ) captured at 300 fps and replayed 40 times slower at 7.5 fps. (Quicktime, 1.1 MB)

MOVIE S2. Receding meniscus motion on structured surface ( $\phi_s = 0.5$ ) captured at 6000 fps and replayed 1000 times slower at 6 fps. (Quicktime, 639 KB)

MOVIE S3. Animation of evolution of the receding meniscus on structured surface ( $\phi_s = 0.5$ ) combining meniscus detected from high-speed images in MOVIE S1-2) (Quicktime, 563 KB)

## Complete References:

1. A. Cassie and S. Baxter, "Wettability of porous surfaces," *Trans. Faraday Soc.*, 1944, **40**, 546–551.
2. R. E. Johnson and R. H. Dettre, in *Contact Angle, Wettability, and Adhesion*, American Chemical Society, 1964, vol. 43, pp. 112–135.
3. C. W. Extrand, "Model for contact angles and hysteresis on rough and ultraphobic surfaces," *Langmuir*, 2002, **18**, 7991–7999.
4. W. Choi, A. Tuteja, J. M. Mabry, R. E. Cohen, and G. H. McKinley, "A modified Cassie-Baxter relationship to explain contact angle hysteresis and anisotropy on non-wetting textured surfaces," *J. Colloid Interface Sci.*, 2009, **339**, 208–216.
5. R. Raj, R. Enright, Y. Zhu, S. Adera, and E. N. Wang, "Unified Model for Contact Angle Hysteresis on Heterogeneous and Superhydrophobic Surfaces," *Langmuir*, 2012, **28**, 15777–15788.
6. M. Reyssat and D. Quéré, "Contact Angle Hysteresis Generated by Strong Dilute Defects," *J. Phys. Chem. B*, 2009, **113**, 3906–3909.
7. R. Dufour, M. Harnois, V. Thomy, R. Boukherroub, and V. Senez, "Contact angle hysteresis origins: investigation on super-omniphobic surfaces," *Soft Matter*, 2011, **7**, 9380–9387.
8. R. Dufour, M. Harnois, Y. Coffinier, V. Thomy, R. Boukherroub, and V. Senez, "Engineering sticky superomniphobic surfaces on transparent and flexible PDMS substrate," *Langmuir*, 2010, **26**, 17242–17247.
9. C. Dorrier and J. Rühe, "Advancing and receding motion of droplets on ultrahydrophobic post surfaces," *Langmuir*, 2006, **22**, 7652–7657.
10. A. Shastry, S. Abbasi, A. Epilepsia, and K.-F. Bohringer, in *International Solid-State Sensors, Actuators and Microsystems Conference (Transducers '07)*, 2007, pp. 599–602.
11. A. T. Paxson and K. K. Varanasi, "Self-similarity of contact line depinning from textured surfaces," *Nat. Commun.*, 2013, **4**, 1492.
12. C. Priest, T. W. Albrecht, R. Sedev, and J. Ralston, "Asymmetric wetting hysteresis on hydrophobic microstructured surfaces," *Langmuir*, 2009, **25**, 5655–5660.
13. D. Öner and T. J. McCarthy, "Ultrahydrophobic surfaces. Effects of topography length scales on wettability," *Langmuir*, 2000, **16**, 7777–7782.
14. W. C. Nelson and C.-J. Kim, "Droplet Actuation by Electrowetting-on-Dielectric (EWOD): A Review," *J. Adhes. Sci. Technol.*, 2012, **26**, 1747–1771.
15. S. Sharma, M. Srisa-Art, S. Scott, A. Asthana, and A. Cass, in *Microfluidic Diagnostics*, eds. G. Jenkins and C. D. Mansfield, Humana Press, Totowa, NJ, 2013, vol. 949, pp. 207–230.
16. S. T. Larsen and R. Taboryski, "A Cassie-like law using triple phase boundary line fractions for faceted droplets on chemically heterogeneous surfaces," *Langmuir*, 2009, **25**, 1282–1284.
17. W. Chen, A. Y. Fadeev, M. C. Hsieh, D. Öner, J. Youngblood, and T. J. McCarthy, "Ultrahydrophobic and Ultralyophobic Surfaces: Some Comments and Examples," *Langmuir*, 1999, **15**, 3395–3399.
18. J. F. Joanny and P.-G. de Gennes, "A model for contact angle hysteresis," *J. Chem. Phys.*, 1984, **81**, 552–562.

19. A. Gauthier, M. Rivetti, J. Teisseire, and E. Barthel, "Role of kinks in the dynamics of contact lines receding on superhydrophobic surfaces," *Phys. Rev. Lett.*, 2013, **110**, 046101.
20. L. Gao and T. J. McCarthy, "Wetting 101°," *Langmuir*, 2009, **25**, 14105–14115.
21. Z. Chen and C.-J. Kim, in *Proc. Int. Conf. Miniaturized Systems for Chemistry and Life Sciences ( $\mu$ TAS)*, Jeju, Korea, 2009, pp. 1362–1364.
22. B. Zhao, J. S. Moore, and D. J. Beebe, "Surface-directed liquid flow inside microchannels," *Science*, 2001, **291**, 1023–1026.
23. G. Sun, T. Liu, P. Sen, W. Shen, C. Gudeman, and C.-J. Kim, "Electrostatic Side-Drive Rotary Stage on Liquid-Ring Bearing," *J. Microelectromechanical Syst.*, 2014, **23**, 147–156.
24. Z. Chen, M.S. thesis, University of California, Los Angeles, 2009.
25. N. A. Patankar, "On the modeling of hydrophobic contact angles on rough surfaces," *Langmuir*, 2003, **19**, 1249–1253.
26. H. Y. Erbil, "The debate on the dependence of apparent contact angles on drop contact area or three-phase contact line: A review," *Surf. Sci. Rep.*, 2014, **69**, 325–365.
27. T. Young, "An Essay on the Cohesion of Fluids," *Philos. Trans. R. Soc. Lond.*, 1805, **95**, 65–87.
28. N. K. Adam and G. Jessop, "Angles of contact and polarity of solid surfaces," *J. Chem. Soc. Trans.*, 1925, **127**, 1863–1868.
29. X. D. Wang, X. F. Peng, J. F. Lu, T. Liu, and B. X. Wang, "Contact angle hysteresis on rough solid surfaces," *Heat Transfer—Asian Res.*, 2004, **33**, 201–210.
30. M. J. Santos and J. A. White, "Theory and simulation of angular hysteresis on planar surfaces," *Langmuir*, 2011, **27**, 14868–14875.
31. W. Xu and C.-H. Choi, "From sticky to slippery droplets: dynamics of contact line depinning on superhydrophobic surfaces," *Phys. Rev. Lett.*, 2012, **109**, 024504.
32. A. Nakajima, Y. Nakagawa, T. Furuta, M. Sakai, T. Isobe, and S. Matsushita, "Sliding of Water Droplets on Smooth Hydrophobic Silane Coatings with Regular Triangle Hydrophilic Regions," *Langmuir*, 2013, **29**, 9269–9275.
33. T. Liu and C.-J. Kim, "Turning a surface superrepellent even to completely wetting liquids," *Science*, 2014, **346**, 1096–1100.
34. R. Dufour, P. Brunet, M. Harnois, R. Boukherroub, V. Thomy, and V. Senez, "Zipping effect on omniphobic surfaces for controlled deposition of minute amounts of fluid or colloids," *Small*, 2012, **8**, 1229–1236.
35. J. W. Krumpfer, P. Bian, P. Zheng, L. Gao, and T. J. McCarthy, "Contact angle hysteresis on superhydrophobic surfaces: an ionic liquid probe fluid offers mechanistic insight," *Langmuir*, 2011, **27**, 2166–2169.
36. J. Zhang and D. Y. Kwok, "Contact Line and Contact Angle Dynamics in Superhydrophobic Channels," *Langmuir*, 2006, **22**, 4998–5004.
37. X. Zhang and Y. Mi, "Dynamics of a Stick–Jump Contact Line of Water Drops on a Strip Surface," *Langmuir*, 2009, **25**, 3212–3218.